CM² MAGAZINE

第 64 期

南方科技大学海洋磁学中心主编

https://cm2.sustech.edu.cn/

创刊词

海洋是生命的摇篮，是文明的纽带。地球上最早的生命诞生于海洋，海洋里的生命最终进化成了人类，人类的文化融合又通过海洋得以实现。人因海而兴。

人类对海洋的探索从未停止。从远古时代美丽的神话传说，到麦哲伦的全球航行，再到现代对大洋的科学钻探计划，海洋逐渐从人类敬畏崇拜幻想的精神寄托演变成可以开发利用与科学研究的客观存在。其中，上个世纪与太空探索同步发展的大洋科学钻探计划将人类对海洋的认知推向了崭新的纬度：深海（deep sea）与深时（deep time）。大洋钻探计划让人类知道，奔流不息的大海之下，埋藏的却是亿万年的地球历史。它们记录了地球板块的运动，从而使板块构造学说得到证实；它们记录了地球环境的演变，从而让古海洋学方兴未艾。

在探索海洋的悠久历史中，从大航海时代的导航，到大洋钻探计划中不可或缺的磁性地层学，磁学发挥了不可替代的作用。这不是偶然，因为从微观到宏观，磁性是最基本的物理属性之一，可以说，万物皆有磁性。基于课题组的学科背景和对海洋的理解，我们对海洋的探索以磁学为主要手段，海洋磁学中心因此而生。

海洋磁学中心，简称 CM^2，一为其全名“Centre for Marine Magnetism”的缩写，另者恰与爱因斯坦著名的质能方程 $E = MC^2$ 对称，借以表达我们对科学巨匠的敬仰和对科学的不懈追求。

然而科学从来不是单打独斗的产物。我们以磁学为研究海洋的主攻利器，但绝不仅限于磁学。凡与磁学相关的领域均是我们关注的重点。为了跟踪反映国内外地球科学特别是与磁学有关的地球科学领域的最新研究进展，海洋磁学中心特地主办 CM^2 Magazine，以期与各位地球科学工作者相互交流学习、合作共进！

“海洋孕育了生命，联通了世界，促进了发展”。 21 世纪是海洋科学的时代，由陆向海，让我们携手迈进中国海洋科学的黄金时代。

目　　录

文献速递

1. 中全新世时期外部强迫机制控制北大西洋沿岸上升流区域

翻译人：仲义 zhongy@sustech.edu.cn

Armand Hernandez, Mario Cachao, Pedro Sousa., et al. ***External forcing mechanisms controlling the North Atlantic coastal upwelling regime during the mid-Holocene*** *[J] Geology, 2020, 49(4), 433-437.*

https://doi.org/10.1130/G48112.1.

摘要: 北大西洋东岸上升流区调控着海洋生态系统生产力变化，并对蓝色海洋经济产生重要影响。虽然全球环流模型显示出在人类导致的气候变暖持续加剧会使得高纬度地区季节性上升流的强度和持续时间增加，但是对北大西洋的预测仍然模糊不清。由于海岸上升流记录的时间分辨率较低，人们对自然强迫效应导致的上升流变化影响知之甚少。本文作者通过微古生物替代性指标记录和模型模拟的结果显示在全新世最暖期（ca. 9-5 ka）主要通过大气和海洋动力学估计北大西洋上升流自然变化的贡献。作者发现，与太阳活动和轨道参数相关的北大西洋东部地区产生的频繁高压环境引发了几十年和千年时间尺度上的上升流变化。该发现为人类世之前上升流变化中外部强迫机制的作用提供了新见解，在对中纬度地区上升流活动进行未来预测时必须考虑这一点因素。

ABSTRACT: Nearshore upwelling along the eastern North Atlantic margin regulates regional marine ecosystem productivity and thus impacts blue economies. While most global circulation models show an increase in the intensity and duration of seasonal upwelling at high latitudes under future human-induced warmer conditions, projections for the North Atlantic are still ambiguous. Due to the low temporal resolution of coastal upwelling records, little is known about the impact of natural forcing mechanisms on upwelling variability. Here, we present a microfossil-based proxy record and modeling simulations for the warmest period of the Holocene (ca. 9–5 ka) to estimate

the contribution of the natural variability in North Atlantic upwelling via atmospheric and oceanic dynamics. We found that more frequent high-pressure conditions in the eastern North Atlantic associated with solar activity and orbital parameters triggered upwelling variations at multidecadal and millennial time scales, respectively. Our new findings offer insights into the role of external forcing mechanisms in upwelling changes before the Anthropocene, which must be considered when producing future projections of midlatitude upwelling activity.

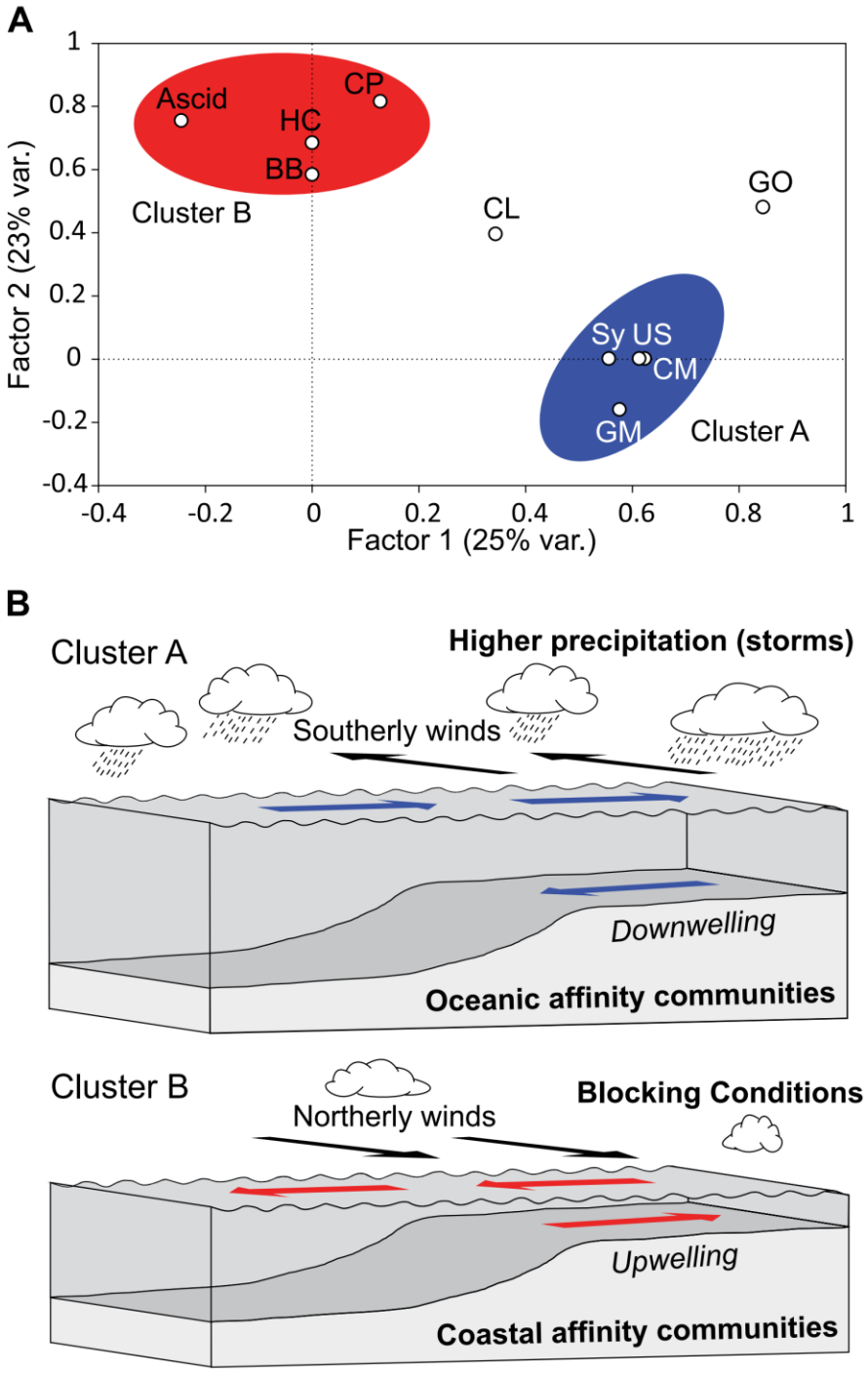

Figure 1. (A) Factor analysis biplot for the Mira estuary (Portugal) records. Defined clusters A (oceanic affinity communities) and B (coastal affinity communities) are indicated by blue and red ellipses, respectively. Lettered taxonomic correspondence: Ascid—ascidians; BB—Braarudosphaera bigelowii; CL—Calcidiscusleptoporus; CM—Coronosphaera mediterranea; CP—Coccolithus pelagicus spp. braarudii; GM—Gephyrocapsa muellerae; GO—Gephyrocapsa Sy—Syracosphaera spp.; US—Umbilicosphaera sibogae. (B) Ideal atmospheric and oceanic conditions for upwelling/ downwelling processes in Iberian North Atlantic margin (INAM) and their relationship with interpretation of factor analysis results. Black arrows indicate most favorable wind direction, whereas colored arrows indicate marine regime (top — downwelling; bottom—upwelling).

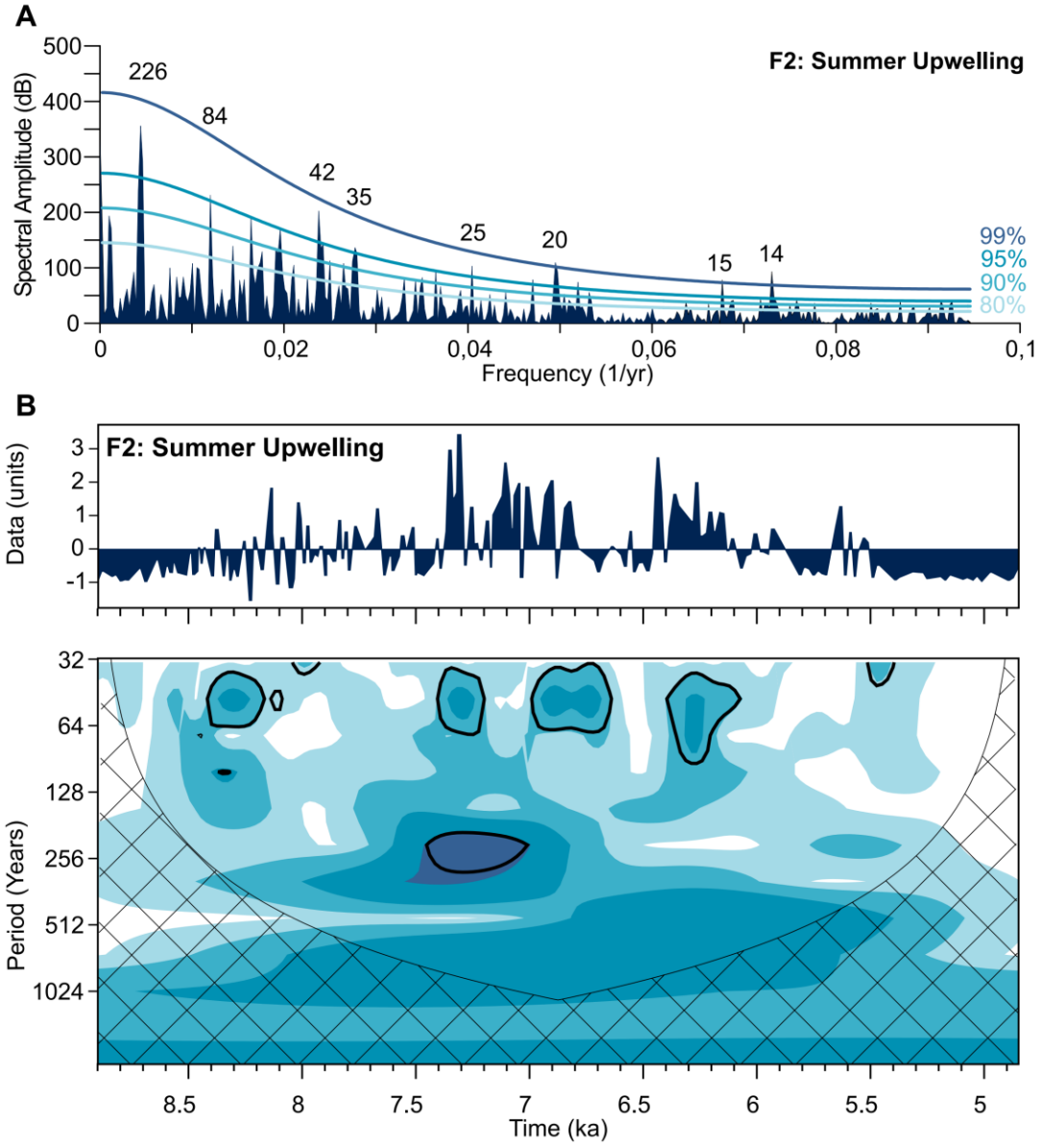

Figure 2. (A) Multitaper analysis of scores from factor 2 for the Mira estuary, Portugal. Confidence levels are shown. (B) Wavelet power spectra of Morlet wavelet analysis on factor 2 scores (lower) as well as respective scores (upper). Blue-scale colors denote power above red noise of 0, 15%, 25%, 50%, and 75%. Black regions are 10% significance regions using red-noise background spectrum. Cross-hatched regions indicate cone of influence.

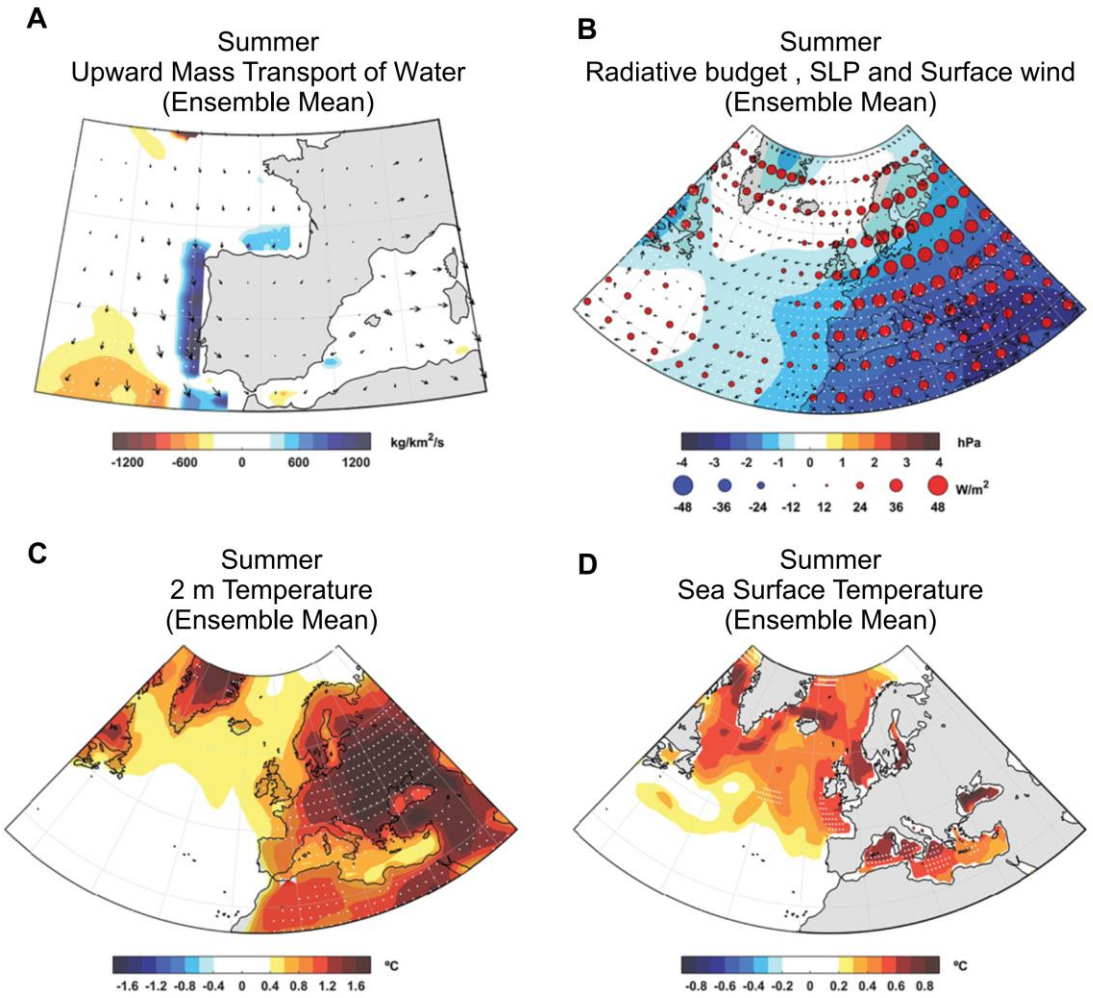

Figure 3. Ensemble of considered PMIP3 models (Paleoclimate Modelling Intercomparison Project, https://pmip.lsce.ipsl.fr/) comparing mid-Holocene to preindustrial control period. (A) Anomalies in upward mass transport of water in 0–150 m layer (shaded) and in surface wind (vectors). (B) Anomalies in surface radiative budget (circles), mean sea-level pressure (SLP; shaded), and surface wind (vectors). (C) Anomalies in 2 m temperature. (D) Anomalies in sea-surface temperatures (SSTs). White stippling denotes areas where high robustness was found for ensemble simulated changes.

2. 早白垩纪通道的演化对形成中的南大西洋和南大洋盆地中的大洋循环和有机碳埋藏的影响

翻译人：李园洁 liyj3@sustech.edu.cn

Dummann W , Steinig S , Hofmann P , et al. ***The impact of Early Cretaceous gateway evolution on ocean circulation and organic carbon burial in the emerging South Atlantic and Southern Ocean basins****[J]. Earth and Planetary Science Letters, 2020, 530:115890.*

https://doi.org/10.1016/j.epsl.2019.115890

摘要：有机碳埋藏是地质和更短事件尺度上的碳循环和气候动力学一个重要驱动力。在早白垩纪冈瓦纳裂解过程形成的洋盆是主要有机碳埋藏地点，说明构造过程和海洋演化可能通过局部有机碳埋藏的变化影响全球气候的趋势和扰动。评估单个洋盆在全球碳气候背景的作用需要了解引起碳埋藏大尺度变化的过程和这些变化的时间。本文作者重建巴列姆阶到阿尔布阶具有全球重要性碳汇的南大西洋和南大洋洋盆的海洋演化和其与有机碳埋藏的联系。本文的重建是基于海水钕同位素和来自多个深海钻孔的沉积学记录以及一个新的大气环流模式。这些洋盆内部和之间的深水循环主要受控于浅的 Falkland Plateau 通道（ ~118Ma-~113Ma）和深的 Georgia Basin 通道（~110 Ma）的开启，对此我们基于生物地层和碳同位素数据提供新的年龄约束。这些通道的开启伴随着局部到盆地有机碳埋藏中减少，表明大洋循环通过深层水流通影响氧化状态。尽管我们的数据没有提供关于区域有机碳埋藏变化对全球碳循环的影响的定量化信息，但阿尔布早期南大西洋盆地中有机碳埋藏减少与全球变暖的同步性表明了强烈的因果关系。

ABSTRACT： Organic carbon burial is an important driver of carbon cycle and climate dynamics on geological and shorter time scales. Ocean basins emerging during the Early Cretaceous break-up of Gondwana were primary sites of organic carbon burial, implying that their tectonic and oceanographic evolution may have affected trends and perturbations in global climate via changes in local organic carbon burial. Assessing the role of individual ocean basins in the global carbon-climate context requires a sound understanding of the processes that induced large-scale changes in carbon burial and the timing of these changes. Here we reconstruct the oceanographic evolution,

and its links to organic carbon burial, in the Barremian to Albian South Atlantic and Southern Ocean basins, which may have acted as carbon sinks of global importance. Our reconstruction is based on combined seawater neodymium isotope and sedimentological records obtained from multiple deep sea drill sites and a new general circulation model. Deep water circulation within and between those basins was primarily controlled by the opening of the shallow Falkland Plateau Gateway (between ~118Ma and ~113Ma) and the deep Georgia Basin Gateway (by ~110Ma), for which we provide new age constraints based on biostratigraphic and carbon isotope data. The opening of these gateways was accompanied by local to basin-wide decreases in organic carbon burial, suggesting that ocean circulation affected the oxygenation state via changes in deep water ventilation. Although our data do not provide quantitative information on the impact of changes in regional organic carbon burial on the global carbon cycle, the synchronicity between the reduction of organic carbon burial in the South Atlantic basin and global warming during the Early Albian points to a strong causal relationship.

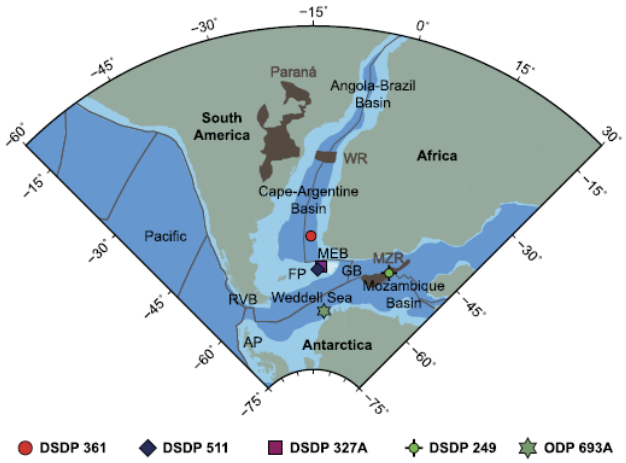

Figure 1. Mid-Aptian (115 Ma) plate tectonic reconstruction of the South Atlantic and Southern Ocean (Matthews et al., 2016). Distribution of land masses (olive green) is based on the modern coastline. Brown shaded areas represent igneous provinces (Paraná large igneous province, Walvis Ridge (WR), and Mozambique Ridge (MZR)) discussed in the text. RVB: Rocas Verdes Basin, AP: Antarctic Peninsula, FP: Falkland Plateau, MEB: Maurice Ewing Bank (white shaded area), GB: Georgia Basin. (For interpretation of the colors in the figure(s), the reader is referred to the web version of this article.).

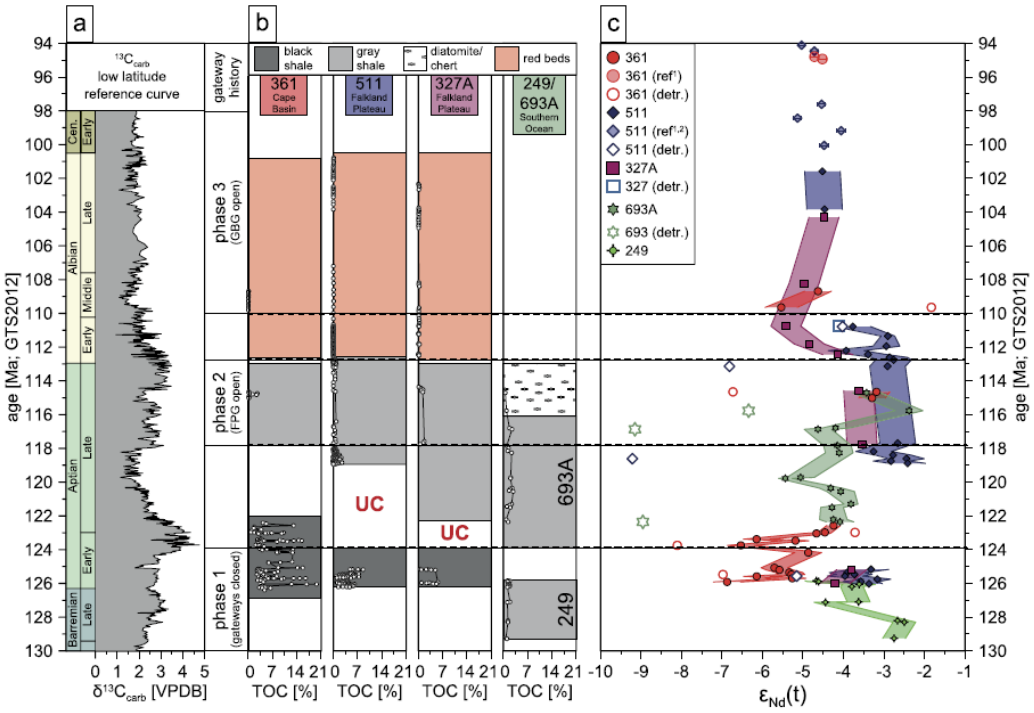

Figure 2. (a) Low latitude carbon isotope record curve compiled by Herrle et al.(2015), (b) total organic carbon contents at DSDP Site 361, DSDP Site 511, DSDP Hole 327A, ODP Hole 693A, and DSDP Site 249 plotted against age. Background shading represents dominant lithology. The height of the lithological columns reflects potential age range of each stratigraphic segment (c) Evolution of seawater Nd isotope signatures (filled symbols) and detrital Nd isotope signatures (open symbols) at all study sites. Shaded areas represent 2SD error ranges of seawater Nd isotope signatures. Late Albian to Cenomanian seawater Nd isotope signatures of DSDP Site 361 and DSDP Site 511 were taken from the literature (ref1: Murphy and Thomas(2013), ref2: Robinson et al.(2010)). Age constraints for literature data were updated to GTS2012 by Moiroud et al.(2016).

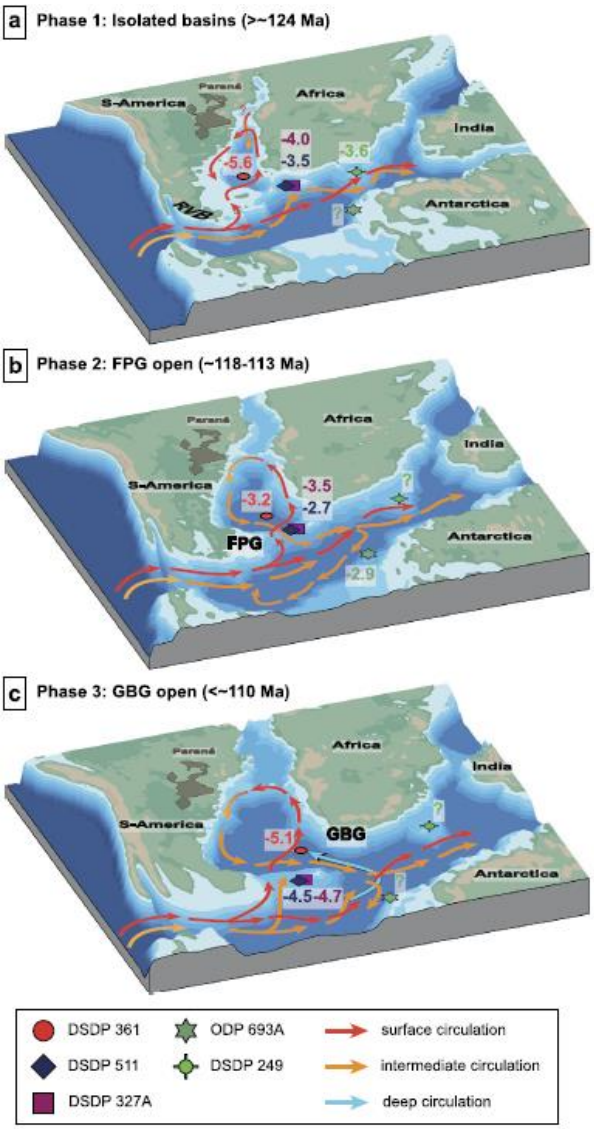

Figure 3. Scheme of the proposed evolution of the circulation system in the Barremian to Albian South Atlantic and Southern Ocean (Please note that the topography shown is idealized and does not claim to be a detailed paleotopographic reconstruction): (a) phase 1 – circulation during the Late Barremian and Early Aptian prior to gateway opening (>~124Ma), (b) phase 2 – circulation after the Falkland Plateau Gateway opened (between 118Ma and 113Ma), (c) phase 3 – circulation after the Georgia Basin Gateway opened (<~110Ma). Numbers next to coring sites represent average seawater ε_{Nd}(t)during each phase. RVB: Rocas Verdes Basin, FPG: Falkland Plateau Gateway, GBG: Georgia Basin Gateway.

3. 铁胶体主导的沉积供应输入大洋内部

翻译人：蒋晓东 jiangxd@sustech.edu.cn

Homoky W B, Conway T M, John S G, et al. ***Iron colloids dominate sedimentary supply to the ocean interior*** *[J]. Proceedings of the National Academy of Sciences of the United States of America, 2021, 118, 13e2016078118.*

https://doi.org/10.1073/pnas.2016078118

摘要：溶解态铁能够调节大洋碳循环，其重要来源是海洋沉积物的溶解。当前对大洋模型中盛行的理解是低含氧量还原作用的机制，而忽略了基于铁同位素证据的额外的海水和孔隙水中非还原的溶解过程。本研究对南大西洋不同水深的浅层孔隙水中胶体铁和溶解态 $\delta^{56}Fe$ 进行分析，结果表明远离低氧系统的造岩胶体产物提供了沉积物的铁源。铁胶体广泛存在这些氧化的沉积物孔隙水中，并且代表了大洋海盆内溶解态 $\delta^{56}Fe$ 的造岩同位素信号。同位素模型实验表明仅在氧化的含氮区域的造岩风化能够形成这些孔隙水铁胶体，而不是沉淀或者络合配位而减少的铁种类。在胶体铁和有机碳丰度之间较宽的协方差表明，有机碳的吸附作用可能控制了纳米级铁矿物的稳定性，主要通过抑制沉积物中铁氢氧氧化物转变为结晶矿物。氧化的大洋沉积物因此可在沉积物-水交换界面能够形成大的有机矿物铁胶体的交换库。这一来源主导了溶解态铁在深海环境中供应，同时还存在大陆架还原态铁供应的路径。

ABSTRACT: Dissolution of marine sediment is a key source of dissolved iron (Fe) that regulates the ocean carbon cycle. Currently, our prevailing understanding, encapsulated in ocean models, focuses on lowoxygen reductive supply mechanisms and neglects the emerging evidence from iron isotopes in seawater and sediment porewaters for additional nonreductive dissolution processes. Here, we combine measurements of Fe colloids and dissolved $\delta^{56}Fe$ in shallow porewaters spanning the full depth of the South Atlantic Ocean to demonstrate that it is lithogenic colloid production that fuels sedimentary iron supply away from low-oxygen systems. Iron colloids are ubiquitous in these

oxic ocean sediment porewaters and account for the lithogenic isotope signature of dissolved Fe ($\delta^{56}Fe$ =+0.07 ± 0.07‰) within and between ocean basins. Isotope model experiments demonstrate that only lithogenic weathering in both oxic and nitrogenous zones, rather than precipitation or ligand complexation of reduced Fe species, can account for the production of these porewater Fe colloids. The broader covariance between colloidal Fe and organic carbon (OC) abundance suggests that sorption of OC may control the nanoscale stability of Fe minerals by inhibiting the loss of Fe(oxyhydr)oxides to more crystalline minerals in the sediment. Oxic ocean sediments can therefore generate a large exchangeable reservoir of organo-mineral Fe colloids at the sediment water interface (a "rusty source") that dominates the benthic supply of dissolved Fe to the ocean interior, alongside reductive supply pathways from shallower continental margins.

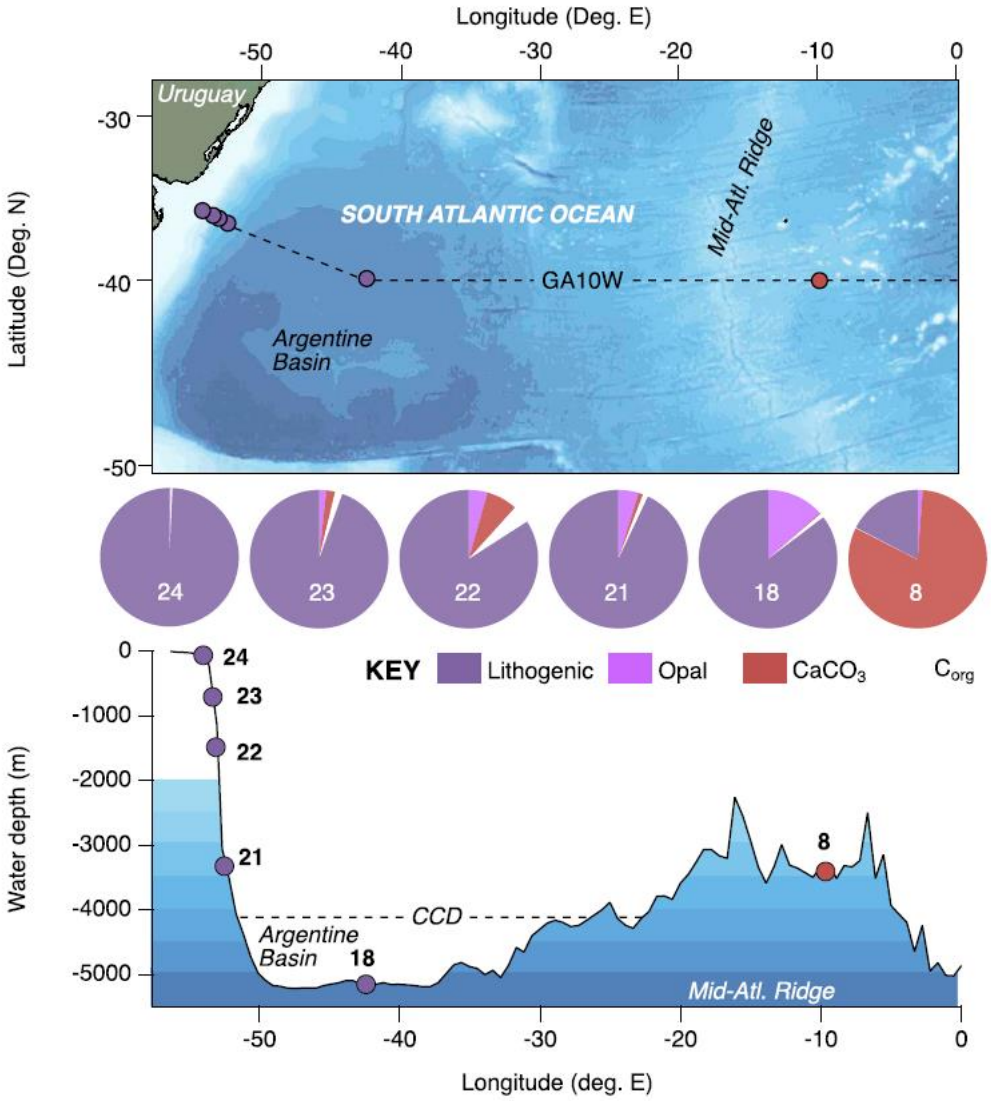

Figure 1. The location and core-top composition of sediment samples collected from GA10W are shown relative to lattitudinal degrees North, longitudinal degrees East and water depth. A blue color index shows 500 m water depth intervals in a plan view (Top) of the study region and a section view (Bottom) along the GA10W sample transect. Sediment classifications of stations 8 to 23 include cohesive silts clays, whereas station 24 is a noncohesive permeable sand. Station 18 lies well beneath the likely $CaCO_3$ compensation depth. Pie charts indicate the mean surface (0 to 5 cmbs) proportions of lithogenic and pelagic components between all sites (SI Appendix, Tables S1 and S2).

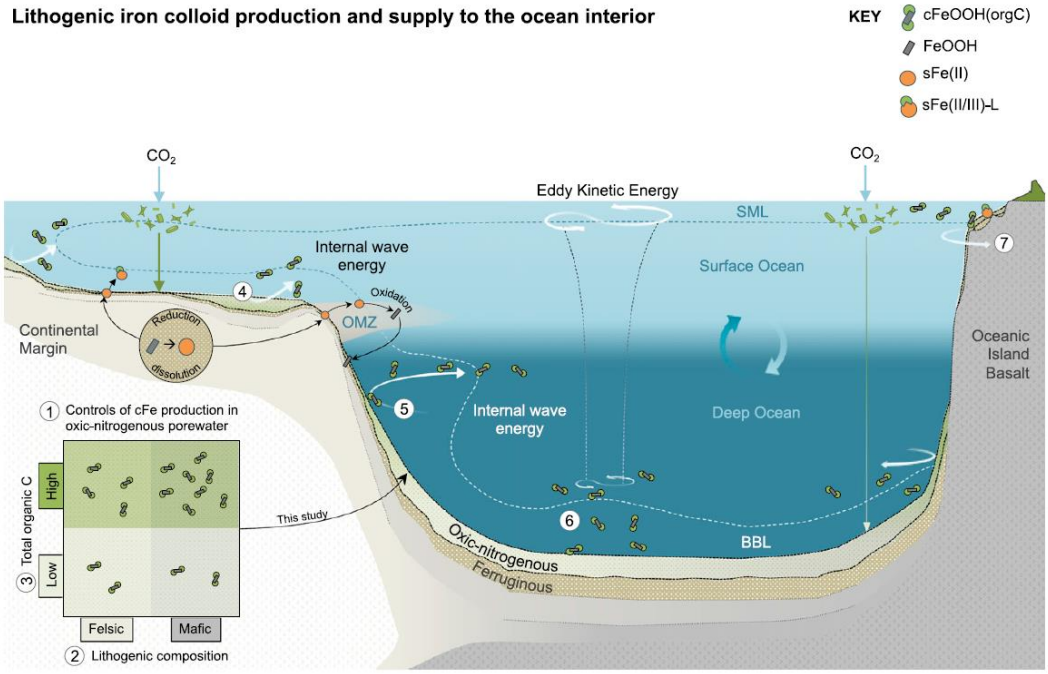

Figure 2. A revised scheme of sedimentary iron supply depicting seven processes that may promote the exchange of lithogenic cFe and isotopes to the ocean interior. 1) The production and diffusion of cFe [depicted as cFeOOH(orgC)] in oxic-nitrogenous ocean sediment porewater; 2) enhanced cFe production from dissolution of mafic minerals; 3) enhanced cFe stabilization by organic C; 4) porewater advection through permeable sediments of the continental shelf (70); 5) entrainment by internal waves and density horizons (16); 6) entrainments by a benthic boundary layer (BBL) coupled to surface ocean eddy kinetic energy (29); and 7) entrainment by the surface mixed layer (SML) and island mass effects (71). The sedimentary release of sFe by RD is restricted to shoaled porewater ferric lines beneath high organic matter flux or oxygen minimum zones (OMZs) in the upper 1,500 m of the ocean and rely on stabilization by organic ligands to resist secondary oxidation and precipitation from the water column (7, 12, 16).

4. 南非 Green Sandstone Bed 碎屑锆石记录了不均一冥古宙地壳与周围地幔的亲缘关系

翻译人：冯婉仪 fengwy@sustech.edu.cn

Drabon N, Byerly B L, Byerly G R, et al. ***Heterogeneous Hadean crust with ambient mantle affinity recorded in detrital zircons of the Green Sandstone Bed, South Africa****[J]. Proceedings of the National Academy of Sciences of the United States of America, 2021, 118: e2004370118.*

https://doi.org/10.1073/pnas.2004370118

摘要：地球早期地壳的性质及其形成过程仍然是前寒武纪地质学的主要问题。由于没有老于 ~ 4.02 Ga 的岩石记录，唯一的直接记录来自罕见的碎屑锆石，并且这些锆石主要来自单一地区：西澳大利亚的 Jack Hills 和 Mount Narryer。在这里，我们报道了在南非 Barberton 绿岩带 Green Sandstone Bed 中新发现的年龄约为 4.15 Ga 的冥古宙碎屑锆石的地球化学特征。结果表明，大部分这些冥古宙锆石的 U-Nb-Sc-Yb 体系显示出与来自现代地幔柱环境的锆石相似的幔源亲缘性，而与来自现代大陆弧或大洋弧的锆石不同。此外，锆石微量元素组成表明，岩浆成分从较高温度的原始成分变化到较低温度的、更演化的、类似英云闪长岩-奥长花岗岩-花岗闪长岩（TTG）的成分，其中演化岩浆的形成经历了一定程度含水地壳的再造作用。我们认为 Green Sandstone Bed 冥古宙锆石的母岩浆形成于基性幔源地壳的重熔，在熔融过程中存在部分含水物质的加入，但其形成过程与现代弧岩浆作用过程不同。

ABSTRACT: The nature of Earth's earliest crust and the processes by which it formed remain major issues in Precambrian geology. Due to the absence of a rock record older than ~ 4.02 Ga, the only direct record of the Hadean is from rare detrital zircon and that largely from a single area: the Jack Hills and Mount Narryer region of Western Australia. Here, we report on the geochemistry of Hadean detrital zircons as old as 4.15 Ga from the newly discovered Green Sandstone Bed in the Barberton greenstone belt, South Africa. We demonstrate that the U-Nb-Sc-Yb systematics of the majority of these Hadean zircons show a mantle affinity as seen in zircon from modern plume-type mantle environments and do not resemble zircon from modern continental or oceanic arcs. The

zircon trace element compositions furthermore suggest magma compositions ranging from higher temperature, primitive to lower temperature, and more evolved tonalite-trondhjemite-granodiorite (TTG)-like magmas that experienced some reworking of hydrated crust. We propose that the Hadean parental magmas of the Green Sandstone Bed zircons formed from remelting of mafic, mantle-derived crust that experienced some hydrous input during melting but not from the processes seen in modern arc magmatism.

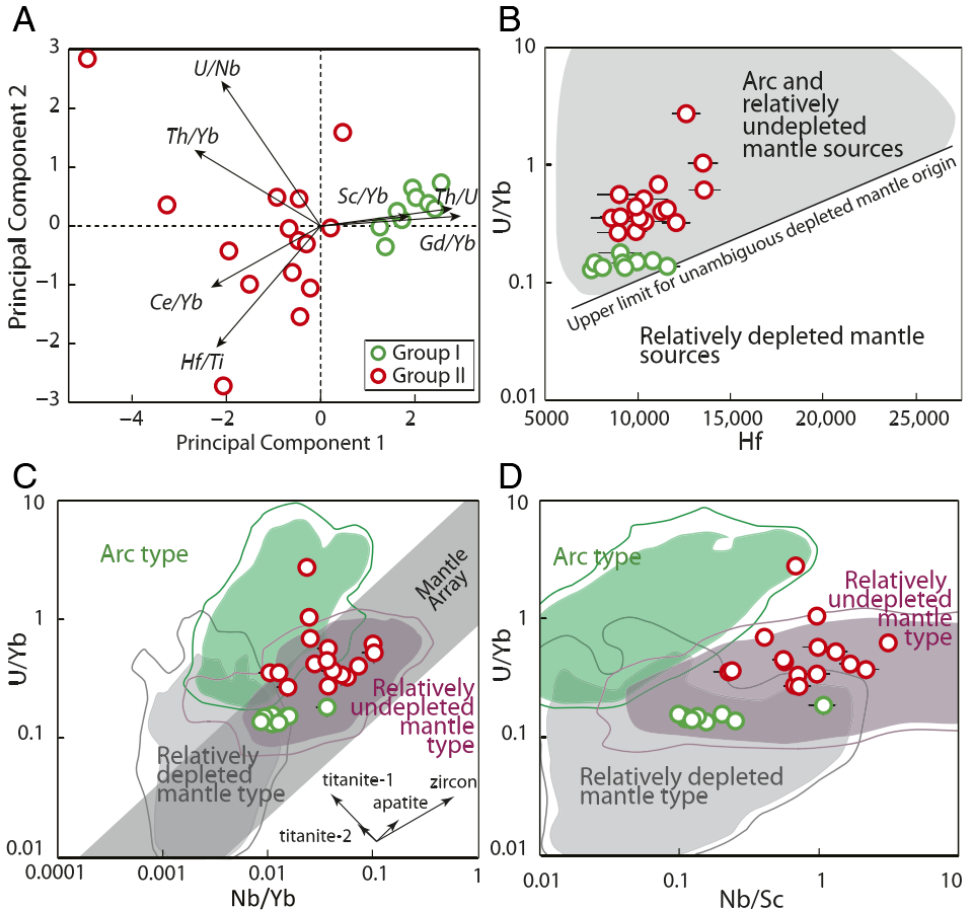

Figure 1. (A) PCA in zircon trace element ratios. Principal component 1 accounts for 51.1% and principal component 2 for 16.1% of the variability. (B and C) Zircon trace element plots modified after Grimes et al. (16). (B) U/Yb ratio versus Hf for zircons from the GSB. (C) U/Yb versus Nb/Yb plot with inset showing the effect of open-system (Rayleigh) fractionation of select minerals on the displayed system (16). (D) U/Yb versus Nb/Sc plot. Colored fields represent a global compilation of zircons from different Phanerozoic tectono-magmatic settings. The outer contour line is shown at the 95% level, which represents the amount of the distribution inside the contour. Green circles represent Group I zircons; red circles represent Group II.

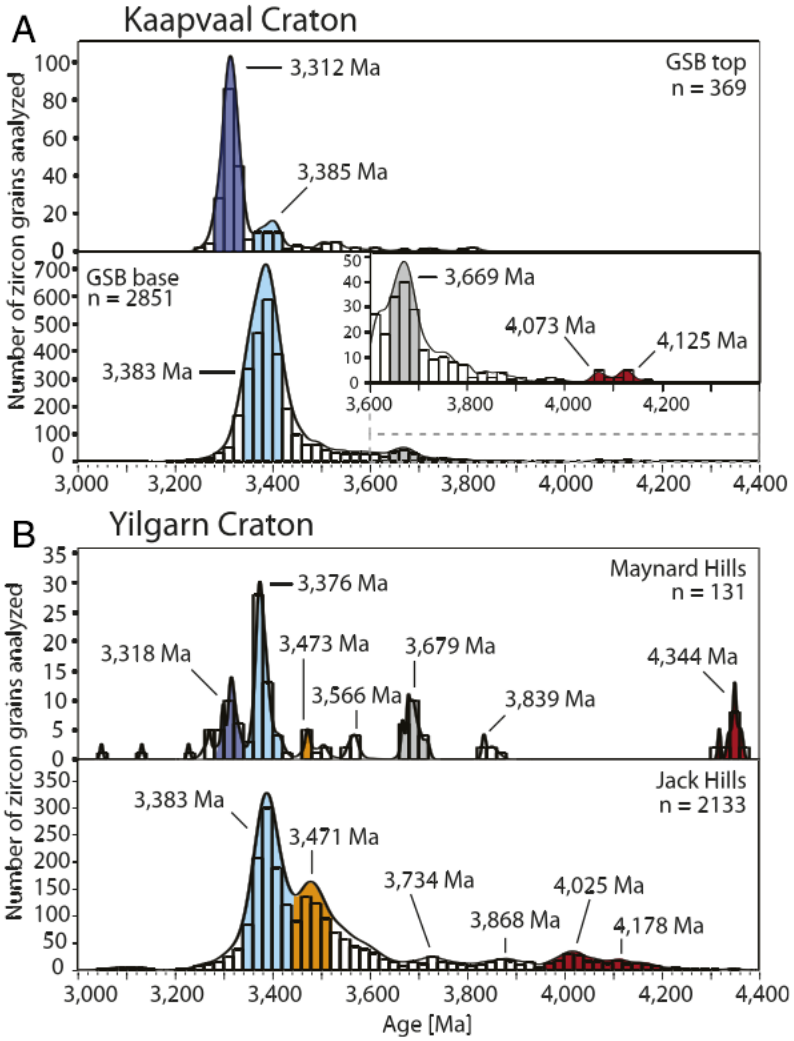

Figure 2. Probability density plots of detrital zircons from (A) the base and the top of the GSB in the Kaapvaal Craton and (B) the Maynard Hills greenstone belt (47), and a representative set of detrital zircon dates from the Jack Hills area (77) in the Yilgarn Craton. Prominent age clusters (colored) were calculated using weighted mean ages and overlap within 2 σ-level.

5. 过去四个间冰期印度洋亚南极南大洋海平面温度

翻译人：张琪 zhangq7@sustech.edu.cn

Shukla S K, Crosta X, Ikehara M. ***Sea surface temperatures in the Indian Sub‐Antarctic Southern Ocean for the last four Interglacial periods [J]****. Geophysical Research Letters, 2021, e2020GL090994.*

https://doi.org/10.1029/2020GL090994

摘要：间冰期（IG）为研究自然气候变化，以及可能存在的比现在更温暖的条件下气候变化的驱动因素提供了很好的契机。然而，南大洋所记录的海平面温度数据十分有限。首个来自南极洲以南印度洋西部的海平面温度数据涵盖了过去四个间冰期，数据表明在海洋同位素 5e 阶段比 9e、7e 和全新世时期更暖。每个间冰期都存在被一个寒冷期打断的两个（早期和晚期）温暖阶段，只有全新世经历了持续的温暖期。早期的温暖阶段可能是由于北方夏季日照的变化与来自北半球和南半球冰盖的反馈，全球海洋环境的变化以及碳循环。反之，晚期的温暖阶段可能是由南半球夏季日照变化引起的。全新世之前千年尺度的海平面温度变化，可能是由于不稳定的温盐环流造成的，导致了两个半球之间更为多变的热量再分配。

ABSTRACT: Interglacial periods (IG) offer an opportunity to understand natural climate variability and its drivers under potential warmer-than-present conditions. However, sea-surface temperature (SST) records from the Southern Ocean (SO) are limited. The first SST record from the SubAntarctic western Indian SO covering the last four IGs suggest warmer conditions during Marine Isotope Stage 5e than 9e, 7e, and Holocene. Each IG presents two (early and late) warm phases interrupted by a cooling, except Holocene that experienced a continuous warming. The early warm phase might be attributable to changes in northern summer insolation with feedbacks from Northern and Southern Hemisphere ice-sheets, global oceanic circulation, and the carbon cycle. Conversely, the late warm phase might be due to changes in Southern Hemisphere summer insolation. Larger millennial-scale SST variability for IGs older than Holocene could be attributed

to a less stable thermohaline circulation, which resulted in more variable heat redistribution between the two hemispheres.

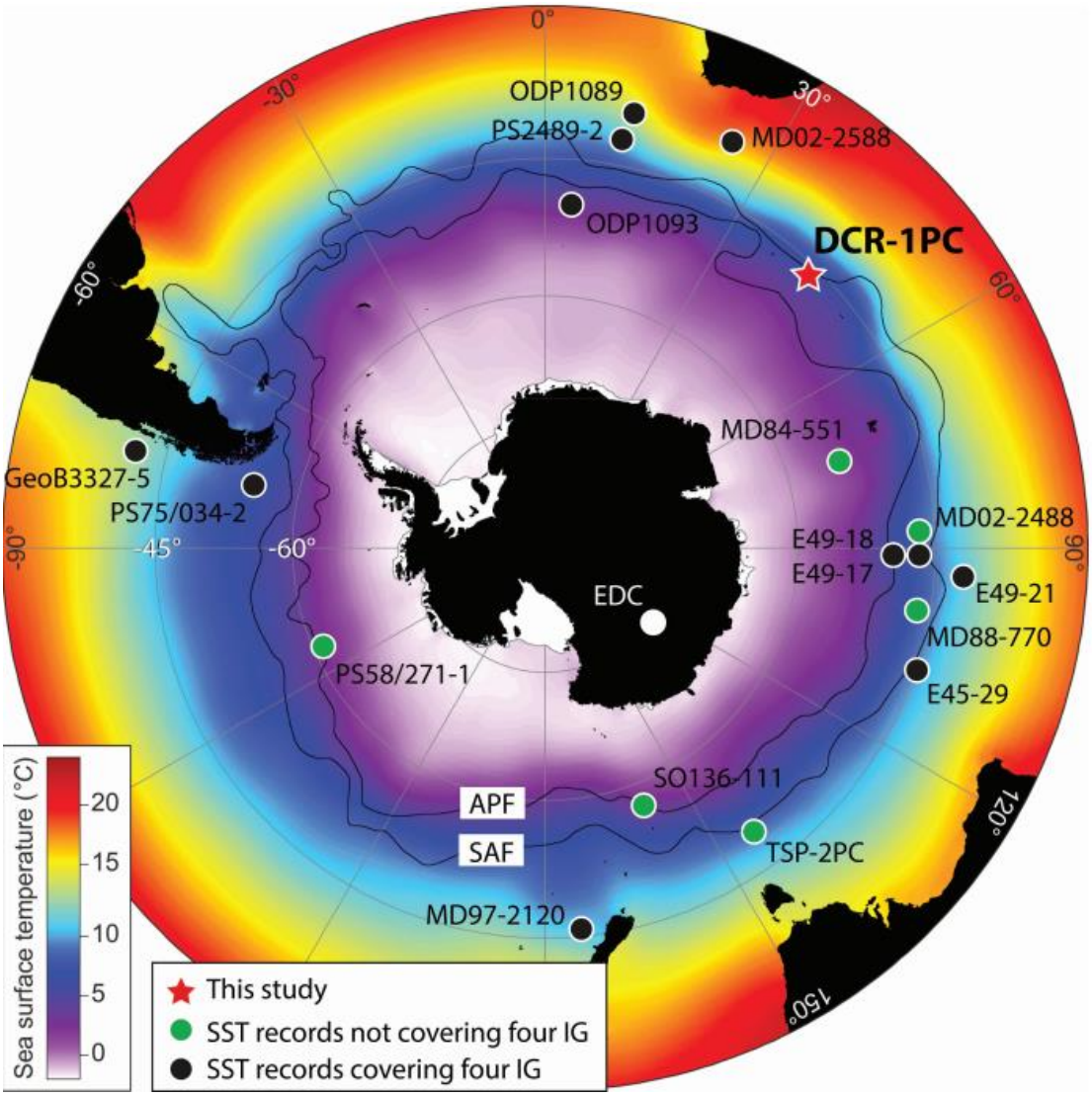

Figure 1. Locations of studied and discussed cores with the background map showing annual mean sea-surface temperature (SST) from the World Ocean Atlas 2013 (Locarnini et al., 2013). New SST data of DCR-1PC (red star) is compared with published SST records covering the past four interglacials (black circles – Howard & Prell, 1992; Becquey & Gersonde, 2003; Pahnke et al., 2003; Cortese et al., 2007; Schneider-Mor et al., 2008; Ho et al., 2012; and Romero et al., 2015) and EDC air temperature (white circle – Bazin et al., 2013). Records covering the past two interglacials are also shown (green circles - Hays et al., 1976; Pichon et al., 1992; Waelbroeck et al., 1995; Labeyrie et al., 1996; Ikehara et al., 1997; Crosta et al., 2004; Govin et al., 2009; and Esper & Gersonde, 2014). APF: Antarctic Polar Front; SAF: Sub-Antarctic Front (Orsi et al., 1995).

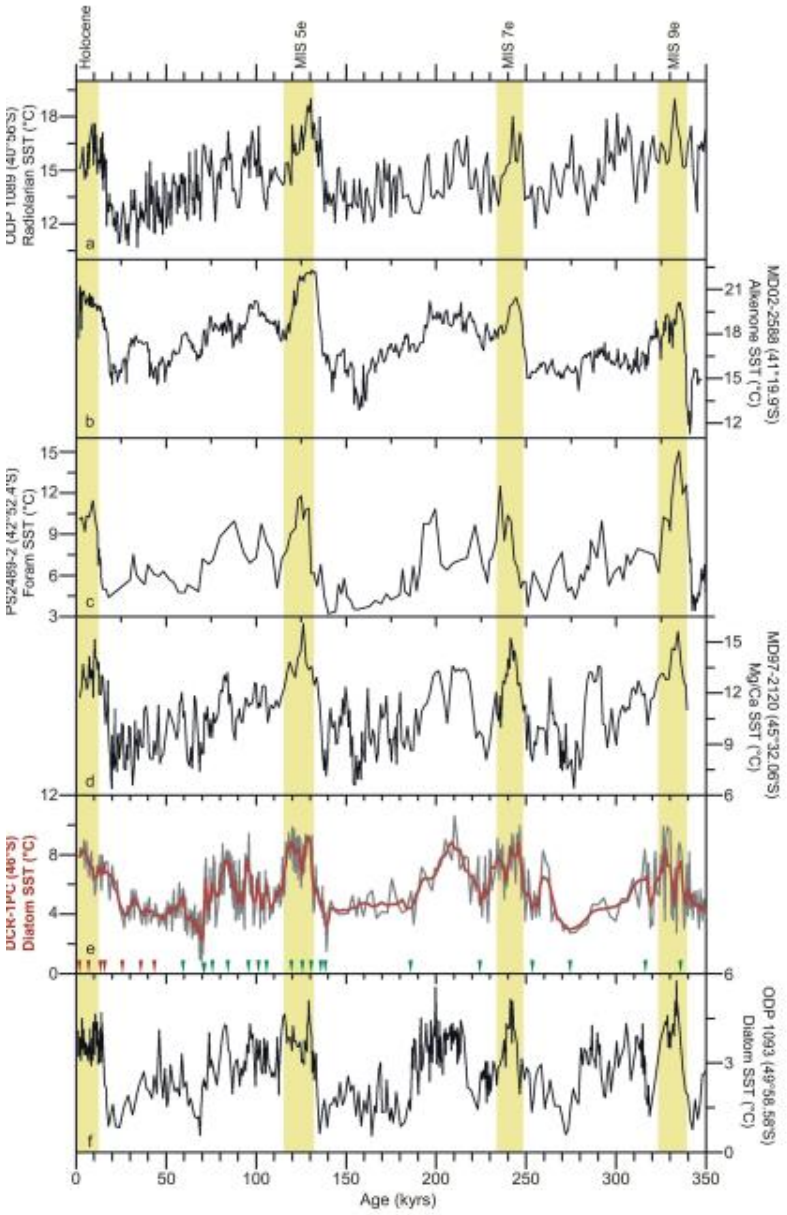

Figure 2. Diatom-based sea-surface temperature (SST) of DCR-1PC core for the past 350 ka with the different interglacial periods highlighted in yellow. The gray curve shows the original SST data, whereas red curve shows SST data smoothed with a 5-point moving average. Age control points along the bottom axis follow ^{14}C AMS dates (red triangles) and tie-points (Crosta et al., 2020) tuned with EPICA Dome C deuterium record. The DCR-1PC SST is compared with ODP Site 1089 from the subtropical Atlantic (Cortese et al., 2007), MD02-2588 core from the Agulhas Plateau (Romero et al., 2015), PS2489-2 core from the sub-Antarctic Atlantic (Becquey & Gersonde, 2003), MD97-2120 core from the subAntarctic Pacific (Pahnke et al., 2003), and ODP Site 1093 from the Atlantic Antarctic Polar Front (Schneider-Mor et al., 2008).

6. 大西洋中脊 13°N 地震活动和拆离断层结构

翻译人：周洋 zhouy3@sustech.edu.cn

R. Parnell-Turner, R.A. Sohn, C. Peirce et al. ***Seismicity trends and detachment fault structure at 13°N, Mid-Atlantic Ridge*** *[J]. Geology, 2021, 49, 320–324.*

https://doi.org/10.1130/G48420.1

摘要：在慢速的扩张脊，板块分离的部分空间通常由长期活动的拆离断层来充填，从而使海底的上地幔和下地壳岩石出露。但是，发生这一过程的机制，地壳结构以及与断层的相互作用仍不太清楚。我们报道了 2016 年在 13° N 附近的大西洋中脊部署的 56 台海底地震仪（OBS）探测结果，包含了两条相邻的拆离断层和两者其间的扩张脊。两条拆离断层是分离的，都表现出较强的地震活动性，它们之间被一个约 8 公里宽的抗震带隔开。线性地震活动带（可能表明岩浆作用）横切了 13° 30′ N 处穹顶状的拆离断层。在更远的南部，在 2016 年的 OBS 与 2014 年进行的调查重叠处，观察到地震活动模式发生了显着变化。这些变化表明，随着板块扩张，拆离断层经历了以前未曾观察到的应力积累及释放的循环。

ABSTRACT: At slow-spreading ridges, plate separation is commonly partly accommodated by slip on long-lived detachment faults, exposing upper mantle and lower crustal rocks on the seafloor. However, the mechanics of this process, the subsurface structure, and the interaction of these faults remain largely unknown. We report the results of a network of 56 ocean-bottom seismographs (OBSs), deployed in 2016 at the Mid-Atlantic Ridge near 13°N, that provided dense spatial coverage of two adjacent detachment faults and the intervening ridge axis. Although both detachments exhibited high levels of seismicity, they are separated by an ~8-km-wide aseismic zone, indicating that they are mechanically decoupled. A linear band of seismic activity, possibly indicating magmatism, crosscuts the 13° 30′ N domed detachment surface, confrming previous evidence for fault abandonment. Farther south, where the 2016 OBS network spatially overlapped with a similar survey done in 2014, signifcant changes in the patterns of seismicity between these surveys are

observed. These changes suggest that oceanic detachments undergo previously unobserved cycles of stress accumulation and release as plate spreading is accommodated.

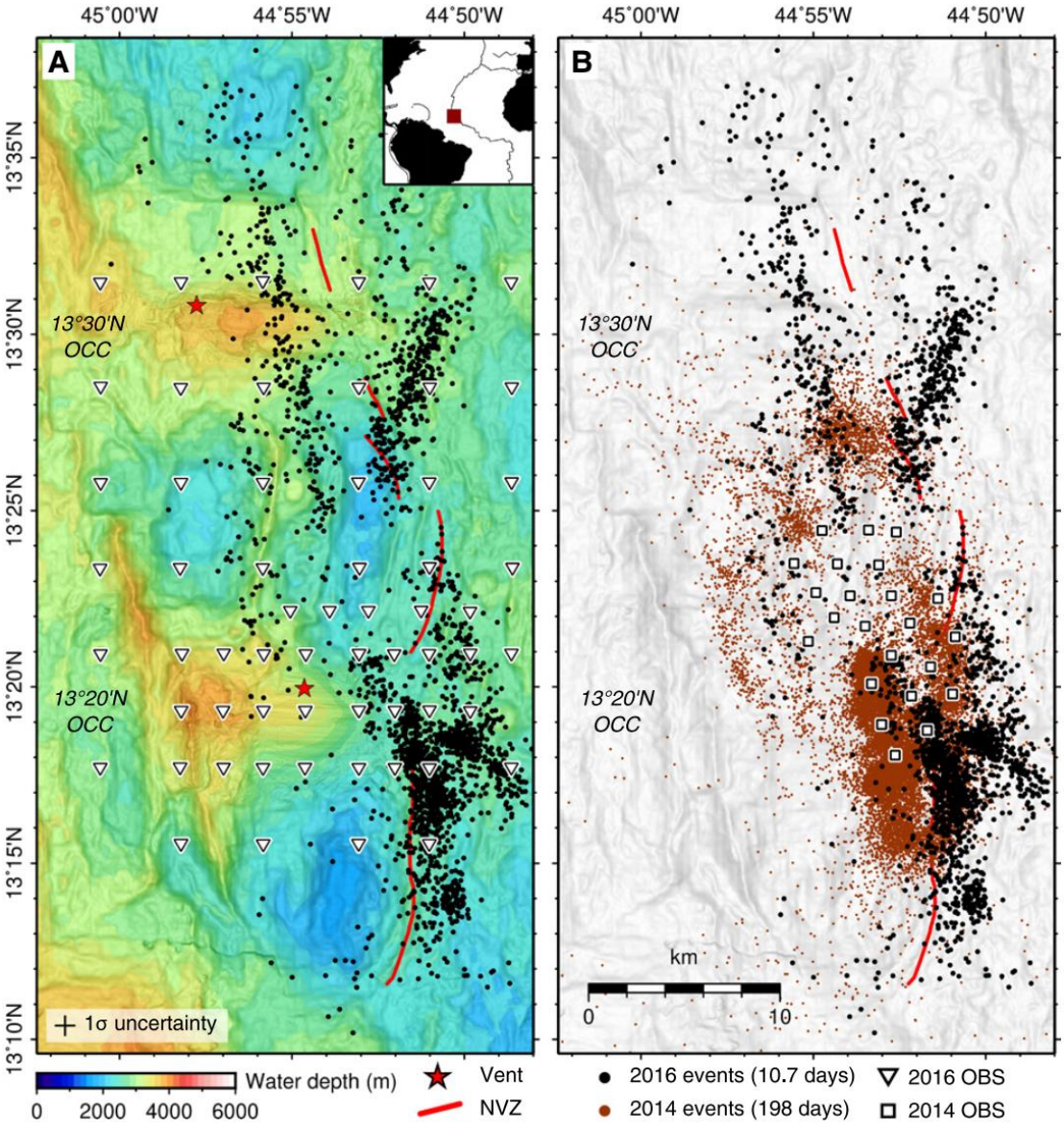

Figure 1. Bathymetry (Searle et al., 2019) and seismicity near 13°20′N, Mid-Atlantic Ridge. (A) Inset shows study site (red box) and plate boundaries (black lines). Black dots are relocated micro-earthquakes recorded by ocean-bottom seismographs (OBSs) (triangles) over ~11 days in 2016; red line is neovolcanic zone (NVZ; Parnell-Turner et al., 2017); red stars are hydrothermal vents. Locations of oceanic core complexes (OCCs) are shown by 13°20′N and 13°30′N labels; cross size is average 68% confdence level in horizontal location uncertainty (0.9 km). (B) Same area as A, with brown dots indicating micro-earthquakes recorded over 198 days in 2014 (squares are OBSs; Parnell-Turner et al., 2017).

7. 台湾恒春增生楔浊积岩沉积记录:对吕宋俯冲体系晚新近纪俯冲速率的指示

翻译人：刘伟 inewway@163.com

Meng X, Shao L, Cui Y, et al. ***Sedimentary records from Hengchun accretionary prism turbidites on Taiwan Island: Implication on late Neogene migration rate of the Luzon subduction system****[J]. Marine and Petroleum Geology, 2021, 124: 104820.*

https://doi.org/10.1016/j.marpetgeo.2020.104820

摘要：虽然菲律宾海板块（PSP）的板块运动模型已经比较好地建立，但它们仍有待于可靠的地质记录来证实。欧亚大陆与 PSP 的斜向汇聚导致了台湾岛沿板块边界的抬升。恒春半岛是台湾最迟出露的地区，具有保存完好的圆状铁镁质砾岩碎屑深海浊积岩。通过源-汇综合分析和广泛的野外地质调查，建立了恒春浊积岩露头与南海钻孔沉积之间的可靠运动学重建模型。根据我们的 U-Pb 年代学(~23.6～25.4 Ma)和元素地球化学结果(正常洋中脊玄武岩)，结合以往的磁异常约束，发现沉积于浊积岩最下部的恒春圆状辉长岩和玄武岩碎屑，与南海洋壳相似。杂基支撑砂岩的多峰 U – Pb 年龄谱显示了物源为越南中部、珠江支流和盆内隆起的混合物源。晚中新世，大量的陆源沉积物从东向流动的康土-莺-琼河和珠江被输送到海底。大规模的浊流冲刷侵蚀了南海中脊，形成了大量的低角度滑脱断层。这些不同来源的物质在进入马尼拉海沟附近的增生楔之前被东移了数千公里。从晚中新世至更新世，PSP 以约 61- 65 mm/yr 的速度向西北移动，促进了增生楔的最终隆起。

ABSTRACT: Although plate motion models for the Philippine Sea Plate (PSP) are relatively well established, they remain to be confirmed by reliable geological records. Oblique convergence between Eurasia and the PSP has resulted in the uplift of Taiwan Island along the plate boundary. As the latest exposed portion of Taiwan, the Hengchun Peninsula features well-preserved deep-sea turbidites with rounded mafic conglomerate clasts. We apply an integrated source-to-sink analysis and broad field investigations to generate a reliable kinematic reconstruction linking the Hengchun

turbidite outcrops with South China Sea (SCS) borehole sediments. Deposited in the lowermost turbidite layer, the Hengchun rounded gabbro and basalt clasts resemble the SCS oceanic crust based on our U–Pb geochronological (~23.6–25.4 Ma) and elemental geochemical results (normal mid-ocean ridge basalts), along with previous magnetic anomaly constraints. The multimodal U–Pb spectra of the matrix-supported sandstones suggest a mixed provenance including central Vietnam, the Pearl River tributaries and potential intrabasinal uplifts, which have not received prior consideration. During the late Miocene, abundant terrigenous sediments from the eastward-flowing "Kontum-Ying-Qiong River" and Pearl River were transported into the submarine environment. The extensive turbidity currents scoured and eroded the SCS mid-ocean ridges, which feature numerous low-angle detachment faults. These materials of various sources were transported eastwards for thousands of kilometers prior to their incorporation into the accretionary prism adjacent to the Manila Trench. From the late Miocene to Pleistocene, the PSP moved northwestward at estimated velocities of ~61–65 mm/yr, facilitating the final uplift and exposure of the accretionary prism.

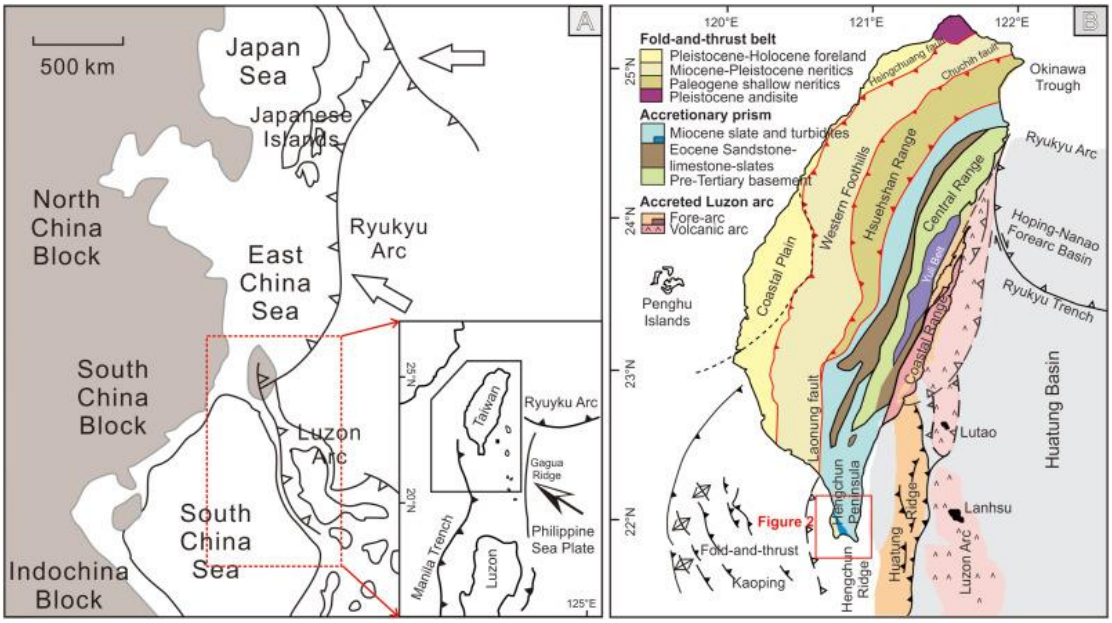

Figure 1. Schematic representation of controls on trench fill and axial-channel evolution. Mod.—moderate; med.—medium.

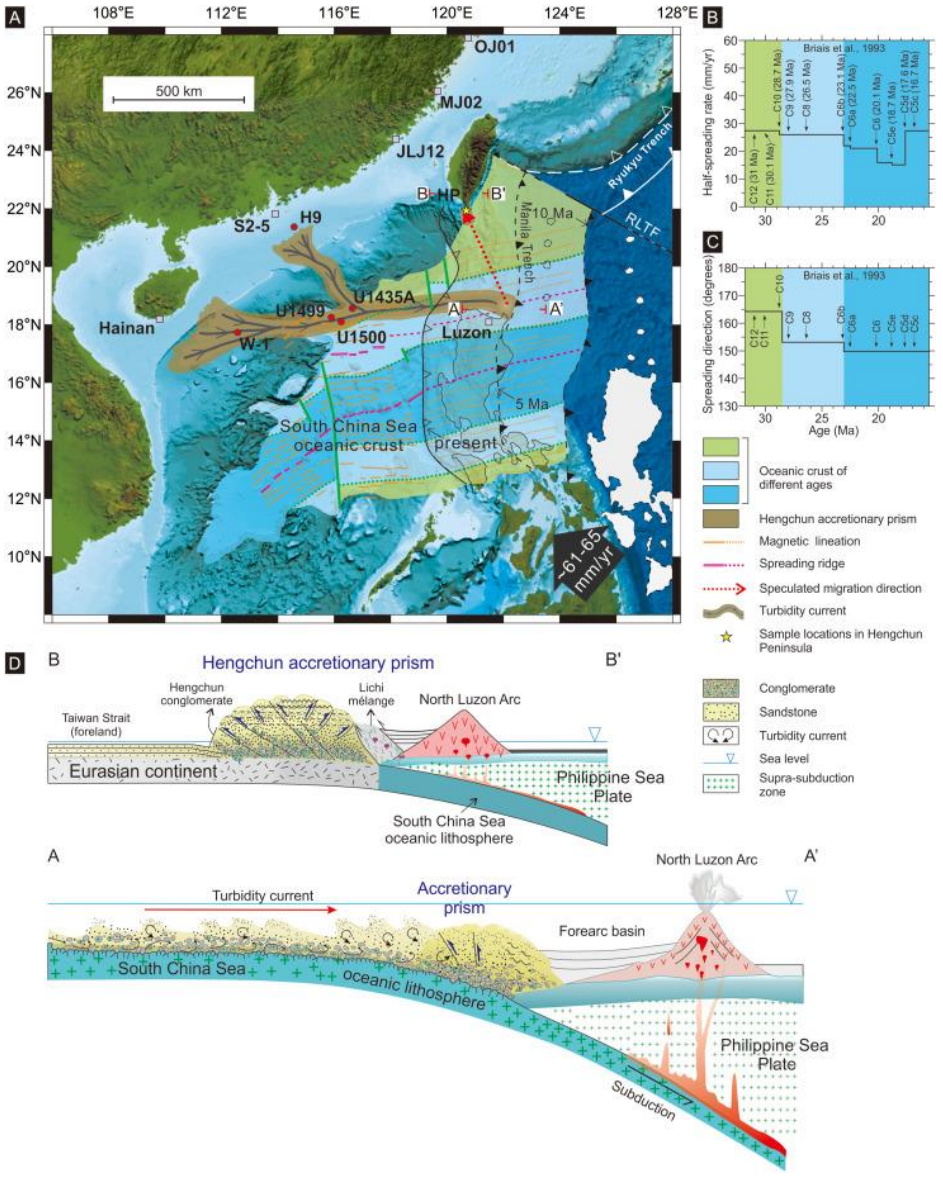

Figure 2. (A) Schematic reconstruction map of the turbidity current across the northern SCS and the final deposition on the Hengchun Peninsula. Presumed paleogeographic locations of the Manila Trench and Luzon Arc are given in the figure (modified after Sibuet et al. (2016) and Wu et al. (2016)). Black dashed lines indicate the present Luzon Arc. Black solid lines indicate the Luzon Arc at approximately 10 and 5 Ma. Dark blue, light blue and green areas separated by green dashed lines mark oceanic domains formed during different kinematic phases, represented by changes in spreading rates, spreading directions or both parameters (Briais et al., 1993). Orange dashed lines show the magnetic anomalies during the SCS oceanic crust extension. Rose red dashed lines show the SCS mid-ocean spreading ridges. Red dots indicate studied or published boreholes representing different source areas. The black bold arrow shows the estimated average speed of the PSP movement relative to the Eurasian Plate. Red dashed lines

indicate migration pathway of the accretionary prism (B) Half-spreading rates are calculated from chrons C12 to C5c using magnetic models from Briais et al. (1993). (C) Spreading directions are calculated based on the assumption that they are perpendicular to the trends of magnetic lineations. (D) Two transects subduction zones in the geographic map (A) are illustrated by geological profiles AA′ and BB’.

8. 使用 FORC-PCA 分析太平洋红粘土中的生物和陆源磁性矿物成分

翻译人：王浩森 11930841@mail.sustech.edu.cn

Yamazaki T, Fu W, Shimono T, et al. ***Unmixing biogenic and terrigenous magnetic mineral components in red clay of the Pacific Ocean using principal component analyses of first-order reversal curve diagrams and paleoenvironmental implications****[J]. Earth, Planets and Space, 2020, 72(1): 1-15.*

https://doi.org/10.1186/s40623-020-01248-5

摘要： 在中纬度的中上层环境中，海底红粘土分布广泛，并可能保留了很长的古海洋学记录。为了对太平洋红粘土进行了磁学研究，以阐明古环境的变化。本文研究了北太平洋西部的三个岩芯和南太平洋的 IODP 孔 U1365A 岩芯。利用一阶反转曲线图（FORC-PCA）的主成分分析揭示了北太平洋西部地区的三个磁性成分（端元 EM1 至 EM3）。 EM1 代表存在相互作用的单畴颗粒（SD）和涡流状态的特征，将其解释为物源输入。 EM2 和 EM3 由具有不同矫顽力分布的非相互作用 SD 颗粒组成，这些颗粒认为是生物来源。 EM1 的相对含量在∽2.7 m 的深度突然增加了，这表明风尘输入增加了。该事件的估计年代约在始新世-渐新世（E / O）边界。透射电子显微镜结果显示，EM2 以等八面体形态的磁小体为主，而 EM3 的子弹形磁小体比例更高。 EM3 的相对贡献从 6.7 至 8.2 m 区间增加，这表明沉积物位于有氧-缺氧过渡带（OATZ），尽管现在岩芯在整个取样深度都是被氧化。 但 OATZ 的化学条件的变化可能是由赤道附近较高的生物生产力引起的。 Hole U1365A 岩芯的 FORC-PCA 确定了两个 EM，陆源（EM1）和生物源（EM2）。在 U1365A 孔处，生物成因组分的矫顽力分布与北太平洋西部的低矫顽性生物成因组分的矫顽力分布相似。在 U1365A 岩芯中，上部的陆源组分突然增加，并且在 E / O 边界附近的年龄特征也很明显。陆源成分增加可能分别是由亚洲和澳大利亚干旱大陆地区的采样点的逐渐构造漂移引起的。或者，风尘的增加可能发生在两个半球的同时期，并且与 E / O 边界的整体变冷有关。

ABSTRACT: Red clay widely occupies the seafloor of pelagic environments in middle latitudes, and potentially preserves long paleoceanographic records. We conducted a rock-magnetic study of Pacific Ocean red clay to elucidate paleoenvironmental changes. Three piston cores from the western North Pacific Ocean and IODP Hole U1365A cores in the South Pacific Ocean were studied here. Principal component analyses applied to first-order reversal curve diagrams (FORC-PCA) reveals three magnetic components (endmembers EM1 through EM3) in a core of the western North Pacific. EM1, which represents the features of interacting single-domain (SD) and vortex states, is interpreted to be of terrigenous origin. EM2 and EM3 are carried by non-interacting SD grains with different coercivity distributions, which are interpreted to be of biogenic origin. The EM1 contribution suddenly increases upcore at a depth of ~ 2.7 m, which indicates increased eolian dust input. The age of this event is estimated to be around the Eocene–Oligocene (E/O) boundary. Transmission electron microscopy reveals that EM2 is dominated by magnetofossils with equant octahedral morphology, while EM3 has a higher proportion of bullet-shaped magnetofossils. An increased EM3 contribution from ~ 6.7 to 8.2 m suggests that the sediments were in the oxic–anoxic transition zone (OATZ), although the core is oxidized in its entire depth now. The chemical conditions of OATZ may have been caused by higher biogenic productivity near the equator. FORC-PCA of Hole U1365A cores identified two EMs, terrigenous (EM1) and biogenic (EM2). The coercivity distribution of the biogenic component at Hole U1365A is similar to that of the lower coercivity biogenic component in the western North Pacific. A sudden upcore terrigenous-component increase is also evident at Hole U1365A with an estimated age around the E/O boundary. The increased terrigenous component may have been caused by the gradual tectonic drift of the sites on the lee of arid continental regions in Asia and Australia, respectively. Alternatively, the eolian increase may have been coeval in the both hemispheres and associated with the global cooling at the E/O boundary.

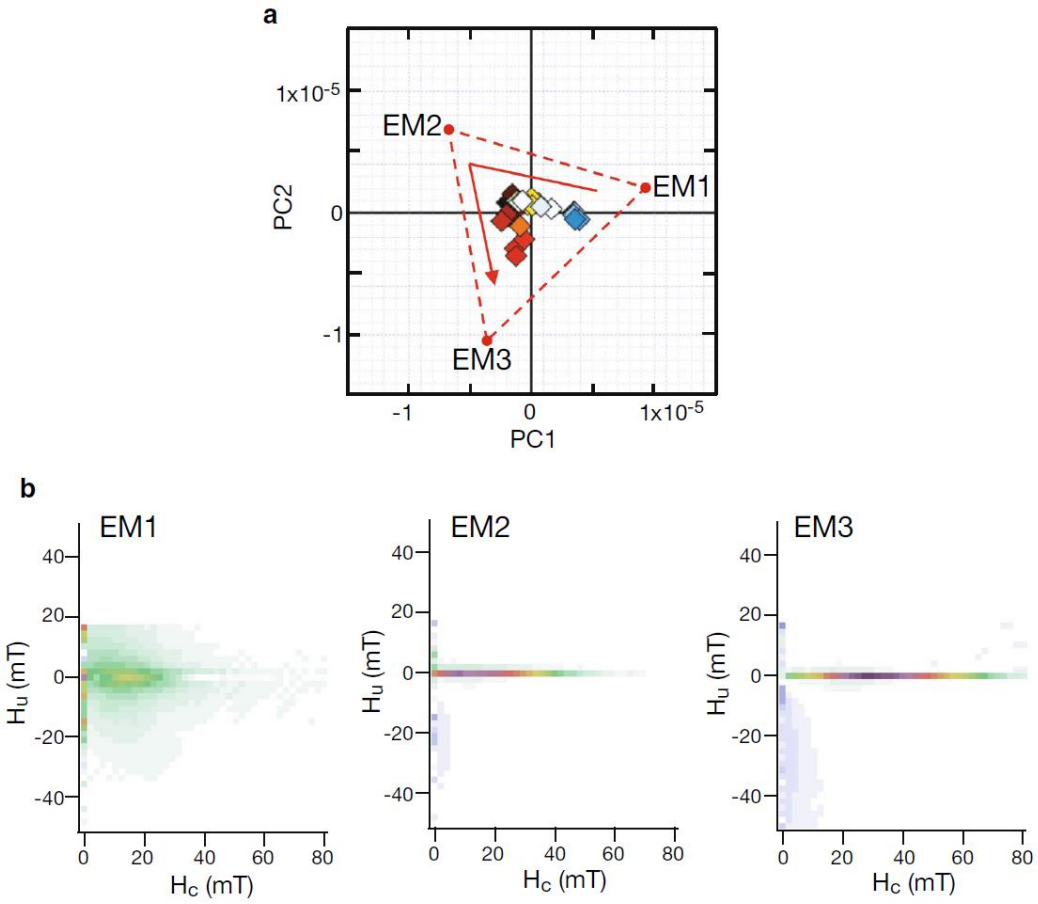

Figure 1. Principal component analysis (PCA) of first-order reversal curve (FORC) diagrams for core KR13-02 PC06. a Distribution of 26 FORC data (squares) on the principal component PC1-PC2 plane. Triangular dashed lines define a three-endmember (EM) system, and the arrow indicates the general downcore trend. b FORC diagrams for EM1, EM2, and EM3.

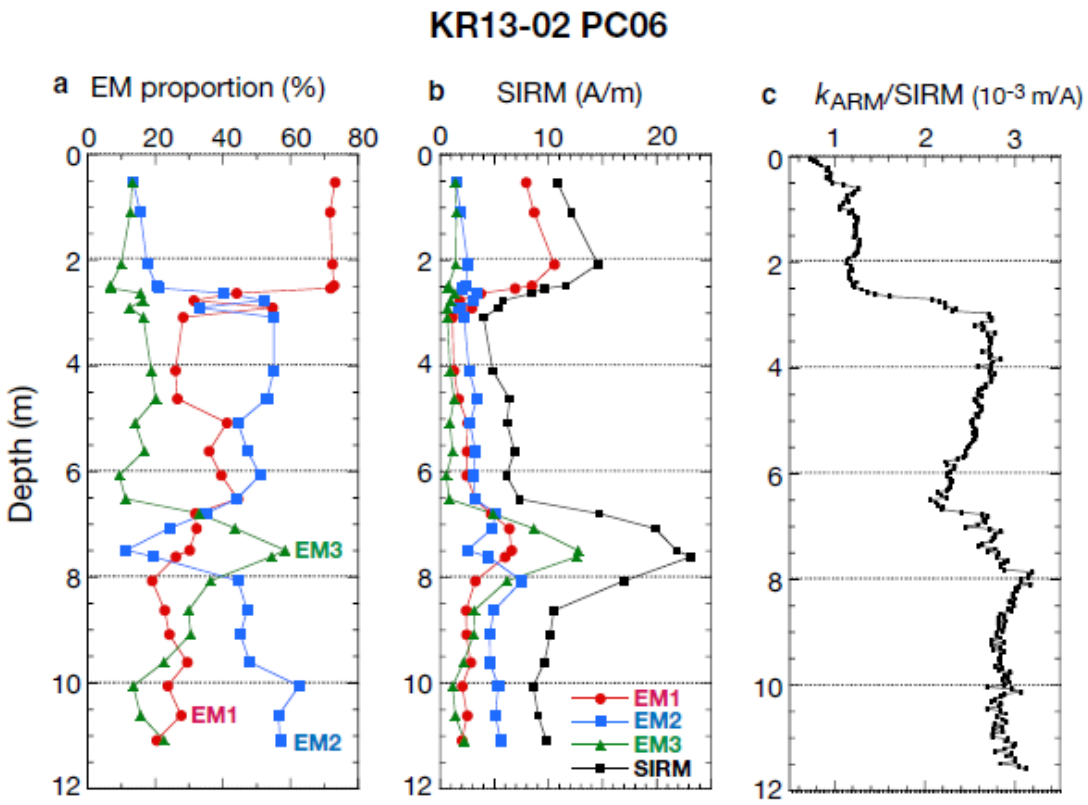

Figure 2. Downcore variations of FORC-PCA endmembers (EMs) and kARM/SIRM for core KR13-02 PC06. **a.** The proportion of EM1 (red), EM2 (blue), and EM3 (green). **b.** SIRM (black) and the contribution to SIRM of individual EMs calculated from the respective proportions. **c.** Variations of kARM/SIRM. Note the synchronous changes of EMs and kARM/SIRM at ~ 2.7 m, and an EM3 increase between ~ 6.7 and 8.2 m.

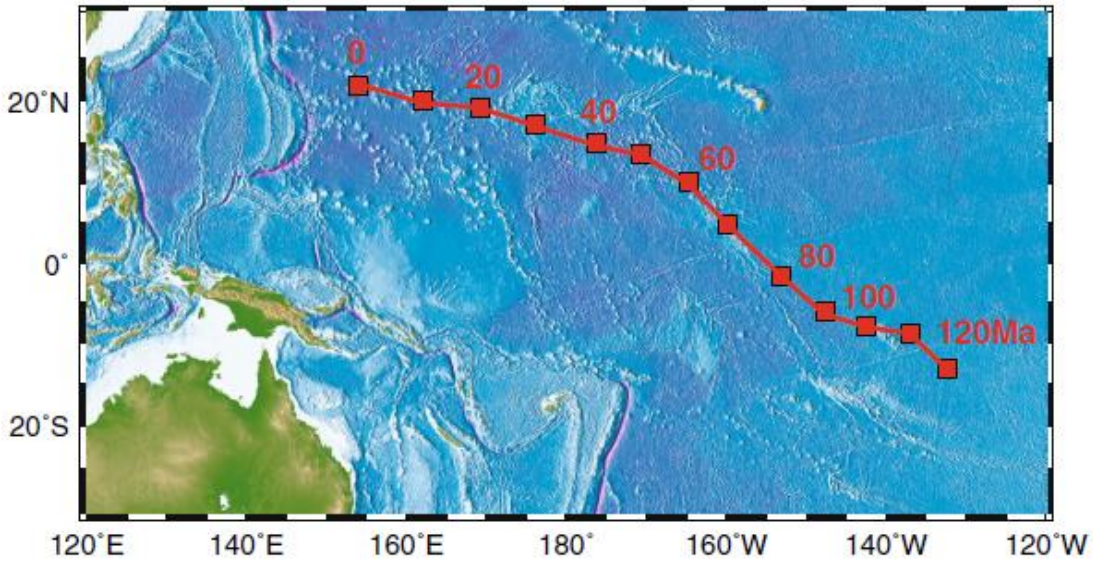

Figure 3. Paleopositions of the core KR13-02 PC06 site superimposed on the present-day bathymetry. The backtrack path was calculated with the GPlates software (Seton et al. 2012).

9. 一种识别岩石磁组构载体的方法

翻译人：李海 12031330@mail.sustech.edu.cn

Elhanati, D, Issachar, R, Levi, T, et al. ***A practical approach for identification of magnetic fabric carriers in rocks****[J]. Journal of Geophysical Research: Solid Earth, 2021, 126, e2020JB021105.*

https://doi.org/10.1022020JB0211059/

摘要：利用磁化率各向异性（AMS）分析岩石的磁组构已是一种的重要手段，已经广泛运用于各种地质和构造环境中。这一方法最大的困难是定义主要的磁相及其相对应的地质解释。作者通过模拟混合磁相（抗磁性、顺磁性、铁磁性）的数据来研究岩石的磁性特征。结果表明，可以通过测量室温和低温的平均磁化率识别主导磁相。在 k_m^{LT}/k_m^{RT} vs k_m^{RT}、k_m^{LT} vs k_m^{RT} 图中展示不同主导磁相的优势区域。作者提出了一种识别主导磁相的方法，即将不同地质条件和主导磁相，在室温、低温下测量的 AMS 结果和 AARM 结果归纳成一个可供参考的标准表。该表的应用使我们有了一个可靠的方式确定主导磁相，并且能快速和可靠地进行地质解释。

ABSTRACT: Magnetic fabric analyses of rocks by Anisotropy of Magnetic Susceptibility (AMS) is a robust petrofabric tool that has been used in varied geological environments and tectonic settings. A fundamental difficulty of this method is to define the dominant magnetic phases and their resulting geological interpretation. We study the magnetic behavior of rocks by simulating data of mixed magnetic phases (i.e. diamagnetic, paramagnetic and ferromagnetic). We show that it is possible to recognize the dominant magnetic phases by measuring the mean susceptibility at room temperature (k_m^{RT}) and at low temperature (k_m^{LT}). Distinct regions of magnetic phase dominancy are demonstrated in k_m^{LT}/k_m^{RT} vs k_m^{RT} and k_m^{LT} vs k_m^{RT} plots. We present a comprehensive approach by coupling the magnetic phase dominancy with possible magnetic fabrics, which are obtained from AMS measured at room and low temperatures (RT-AMS and LT-AMS) and Anisotropy of Anhysteretic Remanent Magnetization (AARM), into a scenario table. Application of this table

allows a robust procedure for determining which magnetic phases are dominant, and permits a fast and reliable geological interpretation in complex settings.

Fabrics RT-AMS	Fabrics LT-AMS	Fabrics AARM	k_m^{RT} [$\times 10^{-6}$ SI]	Case #	LT/RT values	LT vs RT slope	Dominate phases (in k_m^{RT})	RT-AMS carriers
TECTONIC	TECTONIC	TECTONIC	> ~50	I.1	~3.8	~3.8	Para	Para
				I.2	~2.4	~2.4	Para & Ferro	Ferro and/or para / no interpretation
				I.3	~1	~1	Ferro	Ferro
			< ~50	I.4	~0 to 1	~1 to 1.5	Dia	Dia
				I.5	Asymptotical	~3.8	Para & Dia	Para and/or dia / no interpretation
				I.6	Asymptotical	~2.4	Para, Ferro & Dia	Para and/or dia / Ferro and/or dia / All phases / no interpretation
				I.7	Asymptotical	~1	Ferro & Dia	Ferro and/or dia / no interpretation
TECTONIC	TECTONIC	DEPOSITION	> ~50	II.1	~3.2	~3.8	Para	Para
				II.2	~2.1	~2.1	Para & Ferro	Para / no interpretation
				II.3	~1	~1	Ferro	Unlikely fabric
			< ~50	II.4	~0 to 1	~1 to 1.5	Dia	Dia
				II.5	Asymptotical	~3.8	Para & Dia	Para and/or dia / no interpretation
				II.6	Asymptotical	~2.4	Para, Ferro & Dia	Para and/or dia / no interpretation
				II.7	Asymptotical	~1	Ferro & Dia	Dia / no interpretation
TECTONIC	DEPOSITION	TECTONIC	> ~50	III.1	~3.2	~3.8	Para	Unlikely fabric
				III.2	~2.1	~2.1	Para & Ferro	Ferro / no interpretation
				III.3	~1	~1	Ferro	Ferro
			< ~50	III.4	~0 to 1	~1 to 1.5	Dia	Dia
				III.5	Asymptotical	~3.8	Para & Dia	Dia / no interpretation
				III.6	Asymptotical	~2.4	Para, Ferro & Dia	Ferro and/or dia / no interpretation
				III.7	Asymptotical	~1	Ferro & Dia	Ferro and/or dia / no interpretation
TECTONIC	DEPOSITION	DEPOSITION	> ~50	IV.1	~3.2	~3.8	Para	Unlikely fabric
				IV.2	~2.1	~2.1	Para & Ferro	Unlikely fabric
				IV.3	~1	~1	Ferro	Unlikely fabric
			< ~50	IV.4	~0 to 1	~1 to 1.5	Dia	Dia
				IV.5	Asymptotical	~3.8	Para & Dia	Dia / no interpretation
				IV.6	Asymptotical	~2.4	Para, Ferro & Dia	Dia
				IV.7	Asymptotical	~1	Ferro & Dia	Dia / no interpretation
DEPOSITION	DEPOSITION	DEPOSITION	> ~50	V.1	~3.2	~3.8	Para	Para
				V.2	~2.1	~2.1	Para & Ferro	Ferro and/or Para / no interpretation
				V.3	~1	~1	Ferro	Ferro
			< ~50	V.4	~0 to 1	~1 to 1.5	Dia	Dia
				V.5	Asymptotical	~3.8	Para & Dia	Para and/or dia / no interpretation
				V.6	Asymptotical	~2.4	Para, Ferro & Dia	Para and/or dia / Ferro and/or dia / All phases / no interpretation
				V.7	Asymptotical	~1	Ferro & Dia	Ferro and/or dia / no interpretation
DEPOSITION	TECTONIC	DEPOSITION	> ~50	VI.1	~3.2	~3.8	Para	Unlikely fabric
				VI.2	~2.1	~2.1	Para & Ferro	Ferro / no interpretation
				VI.3	~1	~1	Ferro	Ferro
			< ~50	VI.4	~0 to 1	~1 to 1.5	Dia	Dia
				VI.5	Asymptotical	~3.8	Para & Dia	Dia
				VI.6	Asymptotical	~2.4	Para, Ferro & Dia	Ferro and/or dia / no interpretation
				VI.7	Asymptotical	~1	Ferro & Dia	Ferro and/or dia / no interpretation
DEPOSITION	DEPOSITION	TECTONIC	> ~50	VII.1	~3.2	~3.8	Para	Para
				VII.2	~2.1	~2.1	Para & Ferro	Para / no interpretation
				VII.3	~1	~1	Ferro	Unlikely fabric
			< ~50	VII.4	~0 to 1	~1 to 1.5	Dia	Dia
				VII.5	Asymptotical	~3.8	Para & Dia	Para and/or dia / no interpretation
				VII.6	Asymptotical	~2.4	Para, Ferro & Dia	Para and/or dia / no interpretation
				VII.7	Asymptotical	~1	Ferro & Dia	Dia
DEPOSITION	TECTONIC	TECTONIC	> ~50	VIII.1	~3.2	~3.8	Para	Unlikely fabric
				VIII.2	~2.1	~2.1	Para & Ferro	Unlikely fabric
				VIII.3	~1	~1	Ferro	Unlikely fabric
			< ~50	VIII.4	~0 to 1	~1 to 1.5	Dia	Dia
				VIII.5	Asymptotical	~3.8	Para & Dia	Dia
				VIII.6	Asymptotical	~2.4	Para, Ferro & Dia	Dia
				VIII.7	Asymptotical	~1	Ferro & Dia	Dia

Table 1. Coupling the phase dominancy with the mean susceptibility (based on k_m^{LT} and k_m^{RT} values) and RT-AMS, LT-AMS and AARM fabrics. The coupling yields the actual carriers of the RT-AMS fabric, which may be different than the contributor to the mean susceptibility. The model demonstrates applications on sedimentary rocks, however, the same comparative principles may be applied to igneous and metamorphic rocks possessing primary and secondary fabrics.